IEEE Access
Multidisciplinary | Rapid Review | Open Access Journal

Received March 19, 2021, accepted April 5, 2021, date of publication April 8, 2021, date of current version April 16, 2021.

Digital Object Identifier 10.1109/ACCESS.2021.3071715

Analysis of Quadruple Corner-Cut Ridged Elliptical Waveguide by NURBS Enhanced Scaled Boundary Finite Element Method

BINGHAN XUE[1], JIANWEI LEI[1], SHAOKUN MA[2], AND MINGRUI DU[1]
[1]College of Water Conservancy Engineering, Zhengzhou University, Zhengzhou 450001, China
[2]Guangxi Key Laboratory of Disaster Prevention and Engineering Safety, Guangxi University, Nanning 530004, China

Corresponding authors: Jianwei Lei (15333827823@163.com) and Shaokun Ma (mashaokun@sina.com)

This work was supported in part by the Open Research Fund of Water Engineering Materials and Structures, Guangxi Institute of Water Resources Research under Grant GXHRI-WEMS-2020-04, in part by the Systematic Project of Guangxi Key Laboratory of Disaster Prevention and Engineering Safety under Grant 2020ZDK001, in part by the National Key Research and Development Program of China under Grant 2017YFC1501204, and in part by the National Natural Science Foundation of China under Grant 51978630.

ABSTRACT The scaled boundary finite element method(SBFEM) is a semi-analysis method, combing the advantages of boundary element method and finite element method. However, in solving the quadruple corner-cut ridged elliptical(QCRE) waveguide, the traditional SBFEM employ the Lagrange polynomials as the basis functions which leads to the curved boundaries cannot be exactly represented and the continuity order across element is low. In this paper, a non-uniform rational B-spline (NURBS) enhanced SBFEM is firstly extended to solve the QCRE waveguide, which can exactly describe the curved boundaries, reduce the spatial dimensions by one and obtain analytically results in the radial direction. According to its symmetry, only a quarter of the ridged elliptical waveguide needs to be simulated and subdivided into several subdomains. The curved boundaries and straight boundaries of the subdomains are described and discretized by the NURBS and Lagrange basis functions, respectively. The side-face boundaries do not need to be discretized. Then, the NURBS enhanced SBFEM governing equation of the waveguide eigenvalue problem is derived based on the vibrational principle and scaled boundary coordinate transforming. Finally, a generalized eigenvalue equation respecting to the cut-off wave numbers is established by introducing the boundary dynamic stiffness and employing a continued fraction solution. Numerical results verify the high computational efficiency and accuracy of the NURBS enhanced SBFEM with exactly describing the curved boundaries. The influence of the corner-cut on the cut-off wave numbers of several modes and single-mode bandwidth are investigated in details.

INDEX TERMS Scaled boundary finite element method, elliptical waveguide, NURBS basis function, quadruple corner-cut ridge, cut-off wave number.

I. INTRODUCTION

In order to meet the performance requirements of micro-wave and millimeter-wave communication systems, it is necessary to continuously explore and research new waveguides with special cross-section shapes. Due to the characteristics of low cut-off frequency, low impedance and extended bandwidth, various kinds of ridged waveguide have been applied in millimeter-wave and micro-wave communication systems.

The analysis of the waveguide eigenvalue problem is of great significance in designing ridged waveguide devices. Thus, a variety of numerical methods has been used to analyze the characteristics of a ridged waveguide. Such as the magnetic field integral equation (MFIE) method [1], the finite difference method(FDM) [2], meshless method [3], the mode-matching method (MMM) [4], [5], boundary element method (BEM) [6], [7], multipole theory (MT) [8], the finite element method (FEM) [9]–[11], the isogeometric analysis (IGA) [12] and the scaled boundary finite element method(SBFEM) [13], [14]. Among those above mentioned methods, the FEM as the widely used numerical technique has a remarkable capability to solve the ridged waveguide problems. However, the traditional FEM cannot exactly represent the curved boundaries of the computational domain

The associate editor coordinating the review of this manuscript and approving it for publication was Wen-Sheng Zhao.

with low-order basis functions. Besides, the whole computational domain need to be discretized in FEM, which leads to considerable workload in mesh refinement and generation for the complex waveguide problems. Comparing with the traditional FEM, only the boundaries of the unknown domain need to be discretized in BEM, which can reduce the spatial dimension by 1. Hence, the consuming time in mesh generation and CPU time are spared. However, the fundamental solutions of complex waveguide problems are complicated to express.

The SBFEM [15], [16] as a semi-analysis approach has been widely used to analyze different problems, such as fracture mechanics [17]–[19], electromagnetic field [20]–[22], hydraulic structures [23]–[27], heat conduction [28], and so on. The SBFEM inherits the advantages of the BEM and FEM with some unique properties of its own. Such as the fundamental solution is not required, only the boundaries need to be discretized, the governing equations are weakened in the circumferential direction and solved analytically in the radial direction. However, the traditional SBFEM employ the Lagrange polynomials as the basis functions which leads to the curved boundaries cannot be exactly represented and the continuity order across element is low.

Isogeometric analysis (IGA) as an alternative to the conventional FEM was developed by Hughes *et al.* [29], in which NURBS is used to replace conventional Lagrange polynomials. Because the NURBS is employed as a standard approach in CAD systems, the IGA can seamlessly link the CAE model with the CAD model. In the framework of IGA, the geometry can be exactly described by NURBS, and the accuracy of results is superior. The IGA has been extended to solve heat conduction [30], shape optimizing [31], contact problems [32], electromagnetics [33], [34] to name a few.

According to the concept of IGA, the NURBS basis function is used to replace the Lagrange basis function in the traditional SBFEM [35]. The NURBS-based SBFEM has been successfully used in different problems, such as elastostatics problems [36], [37], electrostatic problems [38], heat conduction problems [39] and fracture problems [40]. In this paper, the NURBS enhanced SBFEM is firstly extended to analyze the QCRE waveguide. The NURBS enhanced SBFEM inherits the advantages of IGA and SBFEM, which can exactly describe the curved boundaries, reduce the spatial dimensions by one and obtain analytically results in the radial direction. It worthy note that, the NURBS enhanced SBFEM only employ the NURBS basis function to represent and discretize the curved boundaries of the elliptical waveguide. The side-face boundaries do not need to be discretized. As shown in Fig.1, the QCRE waveguide contains re-entrant corners and curved boundaries. Thus, the NURBS enhanced SBFEM is an attractive approach to solve the QCRE waveguide.

This paper is organized as follows. The concepts of B-splines and NURBS are briefly reviewed in Section II. In Section III, the governing equation of the waveguide eigenvalue problem is derived by the NURBS enhanced SBFEM. A generalized eigenvalue equation is obtained by introducing the boundary dynamic stiffness and employing a continued fraction solution in Section IV. With the NURBS enhanced SBFEM, the QCRE waveguide is solved and discussed in Section V. The conclusions are stated in Section VI.

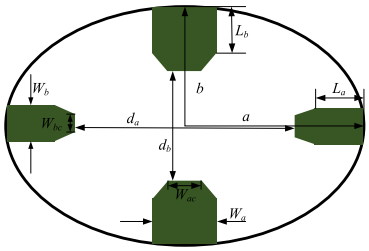

FIGURE 1. The sketch of a quadruple corner-cut ridged elliptical(QCRE) waveguide.

II. B-SPLINES AND NURBS

The concepts of B-Splines and NURBS are briefly outlined in this section. More detailed description can be referred to the literature [29], [41].

A B-Spline basis is defined based on a series of non-decreasing real numbers named knot vector. The knot vector can be written as:

$$\mathbf{s} = \{s_1, s_2, \ldots, s_{n+p+1}\} \tag{1}$$

where s_i is the i th knot, n denotes the number of B-Splines and p denotes the order of B-Splines. The vector $[s_1, s_{n+p+1}]$ is named a single patch and the interval $[s_i, s_{i+1}]$ is named the i-th knot span. The knot vector $\mathbf{s}$ can be named open knot vector, when the first and last knot have a multiplicity of $p+1$ in $\mathbf{s}$. The first and the last basis function have interpolation property at the both ends of the open knot vector. In this paper, the open knot vector is employed.

B-Splines basis functions are defined by the Cox-De Boor formula[41]:

$$\begin{cases} B_{i,0} = \begin{cases} 1, & s \in [s_i, s_{i+1}] \\ 0, & \text{else} \end{cases} \\ B_{i,p} = \dfrac{s - s_i}{s_{i+p} - s_i} B_{i,p-1}(s) \\ \qquad + \dfrac{s_{i+p+1} - s}{s_{i+p+1} - s_{i+1}} B_{i+1,p-1}(s), \ p \geq 1 \end{cases} \tag{2}$$

where, $B_{i,p}$ denotes the i th B-spline basis function with p degree.

Univariate NURBS can be defined by the rational and weighted form of B-spline:

$$R_i^p(s) = \frac{\omega_i B_{i,p}(s)}{\sum_{j=1}^{n} \omega_j B_{j,p}(s)} \tag{3}$$

where $N_{i,p}$ is the i th NURBS basis function with p degree. ω_i denotes the i th weights. The NURBS basis function inherits the advantage of the B-spline basis function, such as non-negativity partition of unity, flexible continuity, local support

and linear independence. NURBS can exactly represent conic sections comparing with the B-splines.

The quadratic NURBS basis function is shown in Fig.2 with an open knot vector $\mathbf{s} = \{0,0,0,0.25,0.50,0.75,1,1,1\}$.

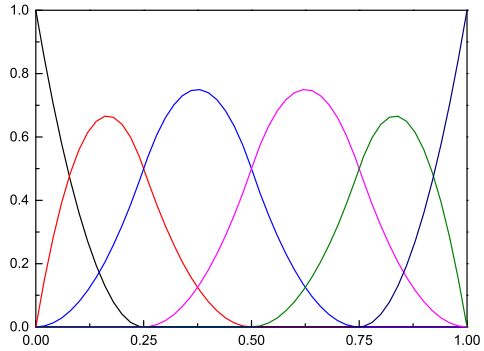

FIGURE 2. Quadratic NURBS functions with open knot vector.

A NURBS curve can be represented as a linear combination of the NURBS basis function:

$$C(s) = \sum_{i=1}^{n} R_i^p(s) P_i \tag{4}$$

where P_i denotes the i th control point.

III. NURBS ENHANCED SBFEM FOR WAVEGUIDE PROBLEMS

For the ridged waveguide with homogeneous permeability and permittivity distributions, the propagation characteristics are determined by the longitudinal component of the magnetic field H_z or electric field E_z. The basic equations of the magnetic field H_z or electric field E_z satisfy the Helmholtz equation:

$$\nabla^2\phi + k_c^2\phi = 0 \tag{5}$$

with essential boundary conditions for TM mode

$$\phi = \bar{\phi} = 0, \quad on\,\Gamma \tag{6}$$

and natural boundary conditions for TE mode

$$\phi_{,n} = \bar{q} = 0, \quad on\,\Gamma \tag{7}$$

where TE mode: $\phi = H_z$. TM mode: $\phi = E_z$. k_c denotes the cut-off wave number which is abbreviated as CWN in the following passage.

As shown in Fig.3, in order to analyze the waveguide eigenvalue problems by using the NURBS enhanced SBFEM, a scaled boundary coordinate system (ξ, η) is establishing. ξ denotes the radial coordinate which ranges from 0 at the scaling center to 1 on the boundary Γ_b, η denotes the circumferential coordinate and a scaling center $O(\hat{x}_0, \hat{y}_0)$ is chosen at a point which satisfies the scaling requirement. The scaling requirement is defined as the whole boundary must be visible from the scaling center.

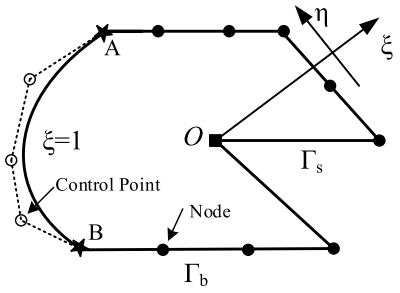

FIGURE 3. A subdomain in the NURBS enhanced SBFEM.

The relationship of the global Cartesian and the scaled boundary coordinate systems can be expressed as:

$$\begin{aligned} \hat{x}(\xi, \eta) &= \xi(x(\eta) - \hat{x}_0)) + \hat{x}_0 \\ \hat{y}(\xi, \eta) &= \xi(y(\eta) - \hat{y}_0)) + \hat{y}_0 \end{aligned} \tag{8}$$

where, $(\hat{x}, \hat{y})$ denotes any point in the domain. $(x(\eta), y(\eta))$ denotes an arbitrary point on the boundary Γ_b.

The gradient operators between the global Cartesian and the scaled boundary coordinate system are related as:

$$\begin{Bmatrix} \frac{\partial}{\partial x} \\ \frac{\partial}{\partial y} \end{Bmatrix} = \mathbf{J}^{-1} \begin{Bmatrix} \frac{\partial}{\partial \xi} \\ \frac{1}{\xi}\frac{\partial}{\partial \eta} \end{Bmatrix} \tag{9}$$

where, $\mathbf{J}$ is independence of ξ named boundary Jacobian matrix:

$$\mathbf{J}(\eta) = \begin{bmatrix} x & y \\ x_{,\eta} & y_{,\eta} \end{bmatrix} \tag{10}$$

The derivative of $\mathbf{J}$ can be written as:

$$\mathbf{J}^{-1}(\eta) = \begin{bmatrix} j_{11} & j_{12} \\ j_{21} & j_{22} \end{bmatrix} = \begin{bmatrix} \boldsymbol{b}_1(\eta) & \boldsymbol{b}_2(\eta) \end{bmatrix} \tag{11}$$

Then, the Laplace operator is expressed as:

$$\nabla = \mathbf{b}_1(\eta)\frac{\partial}{\partial \xi} + \frac{1}{\xi}\mathbf{b}_2(\eta)\frac{\partial}{\partial \eta} \tag{12}$$

As shown in Fig.3, the whole boundary is formed by the side-face boundary Γ_s and the outer boundary Γ_b. Only the outer boundary Γ_b needs to be discretized in the SBFEM, which reduce the spatial dimension by one. In the traditional SBFEM, the whole outer boundary Γ_b is discretized by the Lagrange basis function. Comparing with the traditional SBFEM, the curved segment of the boundary Γ_b is described and discretized by the NURBS basis function and the straight segment of the outer boundary Γ_b is discretized by the Lagrange basis function in the NURBS enhanced SBFEM. As the open knot vector is adopted, then the first and the last basis function have interpolation property at the both ends(A and B in Fig3). Thus, the control points A and B are shared with the straight segment of the outer boundary.

By applying the NURBS enhanced SBFEM to discretize the outer boundary, any point $(x(\eta), y(\eta))$ on the

boundary Γ_b is expressed as:

$$x(\eta) = \mathbf{N}(\eta)\mathbf{x}$$
$$y(\eta) = \mathbf{N}(\eta)\mathbf{y} \tag{13}$$

where the coordinate η ranges from s_i to s_i+1 in each knot span or ranges from -1 to 1 in each Lagrange element. ($\mathbf{x}$, $\mathbf{y}$) represents the coordinates of control points or nodes. $\mathbf{N}(\eta)$ denotes the NURBS or the Lagrange basis functions.

By substituting equation (13) into equation(8), any point in the domain is expressed as:

$$\hat{x} = \xi(\mathbf{N}(\eta)\mathbf{x} - \hat{x}_0) + \hat{x}_0$$
$$\hat{y} = \xi(\mathbf{N}(\eta)\mathbf{y} - \hat{y}_0) + \hat{y}_0 \tag{14}$$

Based on the isoparametric concept, $\phi(\xi, \eta)$ at any point is expressed as:

$$\phi(\xi, \eta) = \mathbf{N}(\eta)\boldsymbol{\phi}(\xi) \tag{15}$$

where $\boldsymbol{\phi}(\xi)$ represents the unknown functions in the radial direction.

Based on the variational principle, the waveguide eigenvalue problem (equations(5),(6) and (7)) can be defined as:

$$\delta\Pi = \delta\left(\frac{1}{2}\int_{\Omega}\left[\left(\frac{\partial\phi}{\partial x}\right)^2 + \left(\frac{\partial\phi}{\partial y}\right)^2 - k_c^2\phi^2\right]d\Omega\right) \tag{16}$$

Substituting equations (12) and (15) into equation (16) yields:

$$\begin{aligned}\delta\Pi = \delta(&\frac{1}{2}\int_{\mathbf{\Omega}}\left(\mathbf{B}_1(\eta)\boldsymbol{\phi}(\xi)_{,\xi} + \frac{1}{\xi}\mathbf{B}_2(\eta)\boldsymbol{\phi}(\xi)\right)^T \\ &\times\left(\mathbf{B}_1(\eta)\boldsymbol{\phi}(\xi)_{,\xi} + \frac{1}{\xi}\mathbf{B}_2(\eta)\boldsymbol{\phi}(\xi)\right)\mathbf{d}\Omega \\ &-\frac{1}{2}\int_{\mathbf{\Omega}} k_c^2\boldsymbol{\phi}(\xi)^T\mathbf{N}(\eta)^T\mathbf{N}(\eta)\boldsymbol{\phi}(\xi)\,\mathbf{d}\Omega = 0\end{aligned} \tag{17}$$

where

$$\mathbf{B}_1(\eta) = \boldsymbol{b}_1(\eta)\mathbf{N}(\eta),\ \mathbf{B}_2(\eta) = \boldsymbol{b}_2(\eta)\mathbf{N}(\eta) \tag{18}$$

By applying the integration by parts to terms with $\delta\boldsymbol{\phi}(\xi)_{,\xi}$ and considering the arbitrariness of $\delta\boldsymbol{\phi}(\xi)$, equation(17) yield:

$$\begin{aligned}&\mathbf{E}_0\xi^2\boldsymbol{\phi}(\xi)_{,\xi\xi} + (\mathbf{E}_0 + (\mathbf{E}_1)^{\mathrm{T}} - \mathbf{E}_1)\xi\boldsymbol{\phi}(\xi)_{,\xi} \\ &\quad -\mathbf{E}_2\boldsymbol{\phi}(\xi) + k_c^2\mathbf{M}_0\boldsymbol{\phi}(\xi) = 0\end{aligned} \tag{19}$$
$$\mathbf{E}_0\boldsymbol{\phi}_{,\xi} + (\mathbf{E}_1)^{\mathrm{T}}\boldsymbol{\phi} = \mathbf{0} \tag{20}$$

where

$$\begin{aligned}\mathbf{E}_0 &= \int_{\Gamma_b}\mathbf{B}_1(\eta)^{\mathrm{T}}\mathbf{B}_1(\eta)\,|\mathbf{J}|\,d\eta \\ \mathbf{E}_1 &= \int_{\Gamma_b}\mathbf{B}_2(\eta)^{\mathrm{T}}\mathbf{B}_1(\eta)\,|\mathbf{J}|\,d\eta \\ \mathbf{E}_2 &= \int_{\Gamma_b}\mathbf{B}_2(\eta)^{\mathrm{T}}\mathbf{B}_2(\eta)\,|\mathbf{J}|\,d\eta \\ \mathbf{M}_0 &= \int_{\Gamma_b}\mathbf{N}(\eta)^{\mathrm{T}}\mathbf{N}(\eta)\,|\mathbf{J}|\,d\eta\end{aligned} \tag{21}$$

Equation (19) is the NURBS enhanced SBFEM equation of the waveguide eigenvalue problem. Equation (20) represents the boundary conditions ($\xi = 1$). $\mathbf{E}_0$, $\mathbf{E}_1$,$\mathbf{E}_2$ and $\mathbf{M}_0$ are the constant coefficient matrix.

IV. THE GENERALIZED EIGENVALUE EQUATION

In order to solve the homogeneous second-order differential equation(19), the concept of "boundary dynamic stiffness" $\mathbf{S}(k_c, \xi)$ is introduced and defined as:

$$\mathbf{Q}(\xi) = \mathbf{S}(k_c, \xi)\boldsymbol{\phi}(\xi) \tag{22}$$

where $\mathbf{Q}(\xi)$ represents the external nodal flux.

According to the principle of virtual work, the relationship between $\mathbf{Q}(\xi)$ and $\boldsymbol{\phi}(\xi)$ is as follows which is similar to equation(20):

$$\mathbf{Q}(\xi) = \mathbf{S}(k_c, \xi)\boldsymbol{\phi}(\xi) = \mathbf{E}_0\xi\boldsymbol{\phi}(\xi)_{,\xi} + (\mathbf{E}_1)^{\mathrm{T}}\boldsymbol{\phi}(\xi) \tag{23}$$

Based on equations(19) and(23), the governing equation in boundary dynamic stiffness can be rewritten as:

$$\begin{aligned}&(\mathbf{S}(k_c) - \mathbf{E}_1)(\mathbf{E}_0)^{-1}\left(\mathbf{S}(k_c) - (\mathbf{E}_1)^{\mathrm{T}}\right) \\ &\qquad + k_c\mathbf{S}(k_c)_{,k_c} - \mathbf{E}_2 + k_c^2\mathbf{M}_0 = 0\end{aligned} \tag{24}$$

Equation(24) belongs to the Riccati differential equation which can be solved by a continued fraction solution[42]. The continued fraction solution has a higher convergence rate and a larger convergence radius than the corresponding power series. Similarly, the continued fraction solution of equation(24) can be expressed as [13], [14]:

$$\mathbf{S}(x) = \mathbf{K} + x\mathbf{M} - \cfrac{x^2}{\mathbf{S}_0^{(1)} + x\mathbf{S}_0^{(1)} - \cfrac{x^2}{\mathbf{S}_0^{(2)} + x\mathbf{S}_0^{(2)} - \cdots - \cfrac{x^2}{\mathbf{S}_0^{(M_{cf})} + x\mathbf{S}_0^{M_{cf}}}}} \tag{25}$$

where $x = -k_c^2$, M_{cf} denotes the order of the continued fraction. $\mathbf{K}$, $\mathbf{M}$, $\mathbf{S}_0^{(i)}$ and $\mathbf{S}_1^{(i)}(i = 1, 2, \ldots, M_{cf})$ denote the coefficient which can be determined by a recursive procedure[42].

Appling the continued fraction solution to equation(25) which is respect to the boundary dynamic stiffness, then the relationship between the flux $\mathbf{Q}$ and the field function $\boldsymbol{\phi}$ can be expressed as:

$$\left(\mathbf{K}_h - k_c^2\mathbf{M}_h\right)\mathbf{y} = \mathbf{F} \tag{26}$$

$$\mathbf{K}_h = diag\left(\mathbf{K}, \mathbf{S}_0^{(1)}, \mathbf{S}_0^{(2)}, \cdots, \mathbf{S}_0^{(M_{cf})}\right)$$

$$\mathbf{M}_h = \begin{bmatrix} \mathbf{M} & -\mathbf{I} & \mathbf{0} & \cdots & \mathbf{0} \\ -\mathbf{I} & \mathbf{S}_1^{(1)} & -\mathbf{I} & \cdots & \mathbf{0} \\ \mathbf{0} & -\mathbf{I} & \mathbf{S}_1^{(2)} & \cdots & \mathbf{0} \\ \vdots & \vdots & \vdots & \ddots & \vdots \\ \mathbf{0} & \mathbf{0} & \mathbf{0} & \cdots & \mathbf{S}_1^{(M_{cf})} \end{bmatrix}$$

$$\mathbf{y} = \left(\boldsymbol{\phi}^T, \left(\boldsymbol{\phi}^{(1)}\right)^T, \left(\boldsymbol{\phi}^{(2)}\right)^T, \ldots, \left(\boldsymbol{\phi}^{(M_{cf})}\right)^T\right)^T$$
$$\mathbf{F} = \left(\mathbf{Q}^T, \mathbf{0}, \mathbf{0}, \cdots, \mathbf{0}\right)^T \quad (27)$$

where $\mathbf{K}_h$ and $\mathbf{M}_h$ are symmetric matrix. $\mathbf{y}$denotes the field function and the auxiliary variables $\boldsymbol{\phi}^{(i)}$. $\mathbf{F}$ denotes the external nodal flux on the outer boundary.

Considering the boundary conditions as expressed in equations(6) and (7) of the homogeneous waveguide eigenvalue problem, $\mathbf{F}$ equals to $\mathbf{0}$ on the right-hand of equation(26). Thus, equation(26) changes to a generalized eigenvalue equation as follows:

$$\left(\mathbf{K}_h - k_c^2 \mathbf{M}_h\right)\mathbf{y} = \mathbf{0} \quad (28)$$

V. NUMERICAL RESULTS

A. THE EXACTNESS OF GEOMETRIC REPRESENTATION

In order to compare the exactness of geometric representation by different basis function, a quarter of ellipse is discretized into four elements by quadratic Lagrange and NURBS basis functions, respectively. A variable L is employed to evaluate the exactness of geometric representation which is defined as $L = (|MF_1| + |MF_2|)/(2a)$, where M denotes the point on the elliptical boundary, F_1 and F_2 means the elliptical focal point, a denotes the lengths of major semi-axes of the ellipse. According to the definition of an ellipse, the exact value of L is one. Fig.4 shows that, the elliptical boundary can be exactly represented by the NURBS basis function, and except the nodal location the elliptical boundary is approximately represented by the Lagrange basis function.

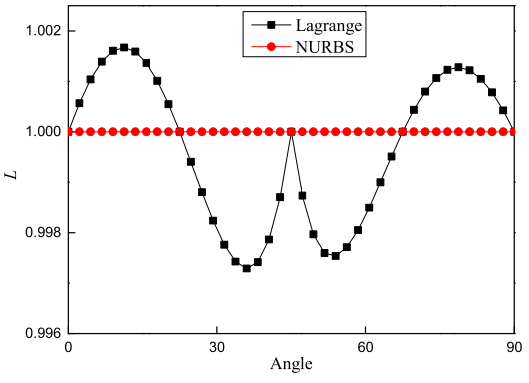

FIGURE 4. The exactness of geometric representation.

B. THE ACCURACY AND EFFICIENCY OF THE NURBS ENHANCED SBFEM

In order to verify the accuracy and efficiency of the NURBS enhanced SBFEM, the normalized cut-off wave number(CWN) $k_c a$ of different modes which consist of the first 4 TM modes and the first 21 TE modes are solved by the traditional SBFEM and the NURBS enhanced SBFEM, respectively. The geometry of the QCRE waveguide assume $a = 10$mm, $c = 0.5a$, $b = (a^2\text{-}c^2)^{0.5}$, $W_a/a = W_b/b = 0.4$ $W_{ac}/W_a = W_{bc}/W_b = 0.5$ and $L_a/a = L_b/b = 0.7$. According to its symmetry, as shown in Fig.5, only a quarter of the QCRE waveguide needs to be simulated and divided to nine subdomains. The curved boundaries and straight boundaries of each subdomain are described and discretized by quadratic NURBS and Lagrange basis functions, respectively. In the analysis, four meshes are employed to validate the convergence of the NURBS enhanced SBFEM. The coarse mesh as shown in Fig.5(b) consists of 16 elements (12 Lagrange elements and 4 NURBS elements) with 31 nodes (24 nodes and 7 control points). Based on the coarse mesh, the other three meshes are constructed by the binary subdivision. The quarter of the QCRE waveguide is also discretized into four meshes(16 elements with 33 nodes, 32 elements with 65 nodes, 64 elements with 129 nodes and 128 elements with 257 nodes) by the traditional SBFEM. In each subdomain, the scaling center is chosen at the same position where satisfy the scaling requirement in the traditional SBFEM and the NURBS enhanced SBFEM. The degree of the continued fraction solution is set as three. Unfortunately, there is no analytical solution of the QCRE waveguide. Thus, a FEM solution[13] with 69217 nodes is employed as a reference. The CPU time is used to verify the efficiency of the NURBS the SBFEM which is recorded on a Windows 10 desktop computer (CPU: Intel core i7-8700 at 3.20 GHz). The root mean square error(RMSE) is chosen to verify the accuracy of the NURBS enhanced SBFEM which is defined as $\left(\sum_{i=1}^{25}\left(\left(k_{c-cal} - k_{c-ref}\right)/k_{c-ref}\right)^2/25\right)^{0.5}$. The normalized CWN, CPU time and RMSE of the ridged elliptical waveguide with the traditional SBFEM and NURBS enhanced

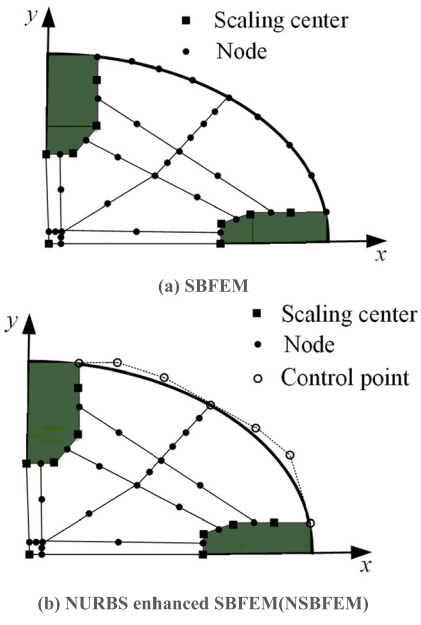

FIGURE 5. The sketch of the discretization mesh.

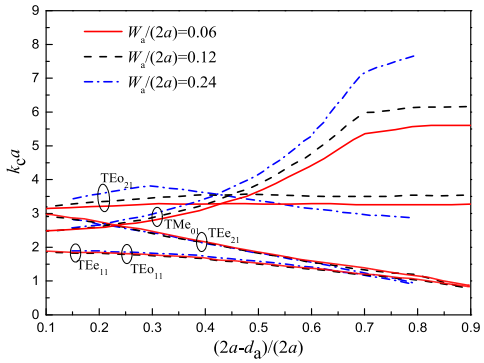

(a) The eccentricity e = 0.1

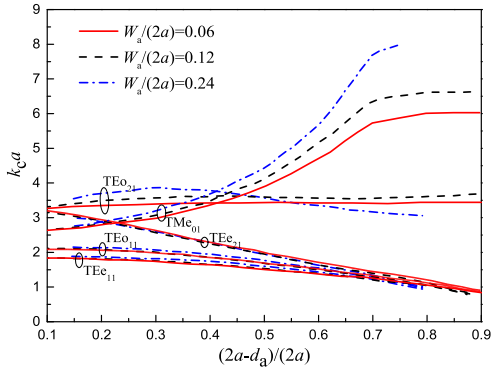

(b) The eccentricity e = 0.5

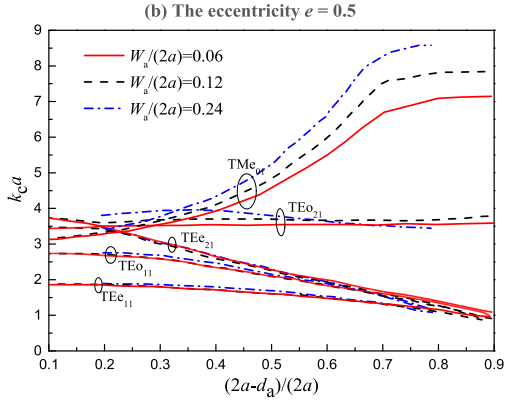

(c) The eccentricity e = 0.75

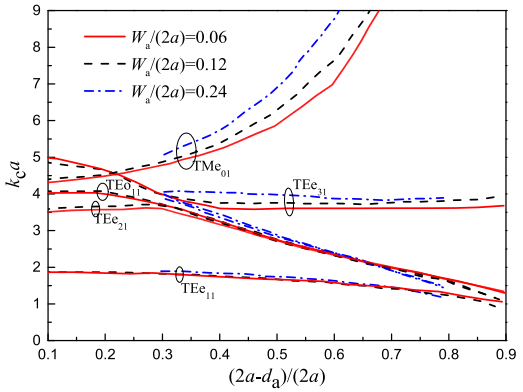

(d) The eccentricity e = 0.9

FIGURE 6. Normalized CWNs versus different ratio of $(2a - d_a)/(2a)$ and $W_a/(2a)$.

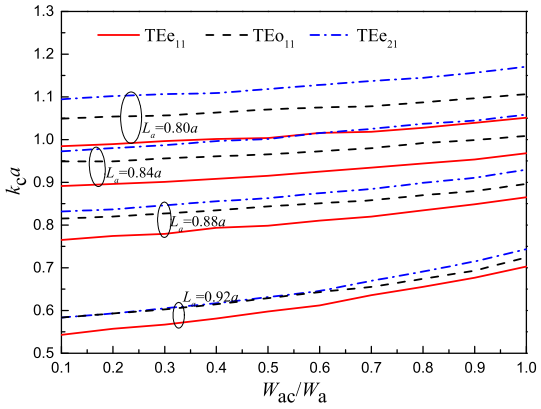

(a) The CWNs of the TEe$_{11}$, TEe$_{21}$ and TEo$_{11}$ modes

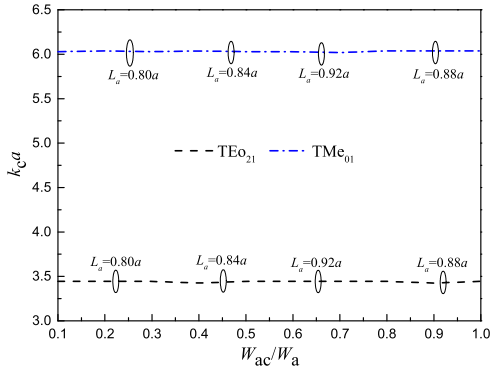

(b) The CWNs of the TMe$_{01}$ and TEo$_{21}$ modes

FIGURE 7. Normalized CWNs versus different L_a/a and W_{ac}/W_a.

SBFEM are given in Tab.1. From Tab.1, the normalized cut-off numbers obtained by the NURBS enhanced SBFEM are in very good agreement with those obtained by the FEM, the accuracy and efficiency of the NURBS enhanced SBFEM are better than that of the traditional SBFEM.

C. THE EFFECT OF THE CORNER-CUT RIDGES ON THE CWNs

Then, the effect of the corner-cut ridges on the CWNs of several lowest modes is analyzed with the NURBS enhanced SBFEM.

With the fixed aspect ratio $W_a/(2a) = W_b/(2b)$, $L_a/a = L_b/b$ and $W_{ac}/W_a = W_{bc}/W_b = 0.5$, the relationship of the normalized CWNs k_ca of TEe$_{11}$, TEe$_{21}$, TEo$_{11}$, TEo$_{21}$, TMe$_{01}$ and TEe$_{31}$ modes with different ratio of eccentricity e, $W_a/(2a)$ and $(2a\text{-}d_a)/(2a)$ is shown in Fig.6.

As shown in Fig.6, with the increasing of $(2a\text{-}d_a)/(2a)$, the normalized CWNs of TEe$_{11}$, TEe$_{21}$ and TEo$_{11}$ modes remain unchanged at first, then decrease and eventually tend to the same value. The effect of the ridge thickness W_a on the normalized CWNs of the TEe$_{11}$, TEe$_{21}$ and TEo$_{11}$ modes is little.

When eccentricity $e = 0.1$, the normalized CWNs of the TEo$_{11}$ mode is very close to that of the TEe$_{11}$ mode. With the increasing of eccentricity e, the normalized CWNs

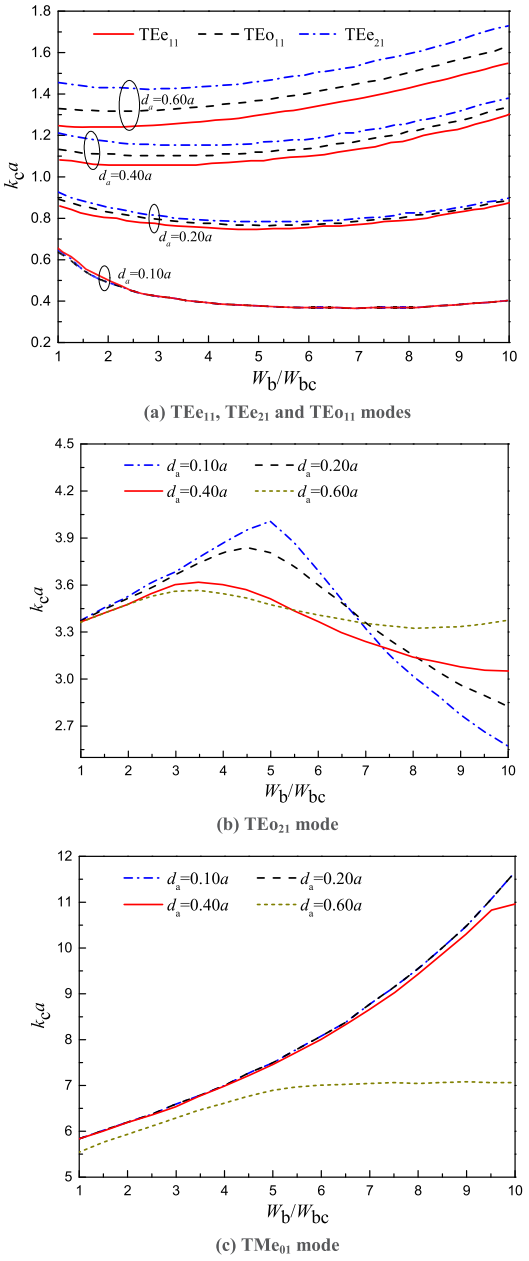

FIGURE 8. Normalized CWNs versus different d_a/a and W_b/W_{bc}.

of the TEo_{11} mode are greater than that of the TEe_{11} mode and even greater than that of TEe_{21} mode. For each eccentricity e, the normalized CWNs of TMe_{01} mode increases with the ridge thickness $W_a/(2a)$ and $(2a\text{-}d_a)/(2a)$ increase.

When eccentricity $e = 0.1$, 0.5 and 0.75, $W_a/(2a) = 0.06$ and 0.12, the normalized CWNs of TEo_{21} mode increase at first and then tend to be flat with the increase of $(2a\text{-}d_a)/(2a)$. When eccentricity $e = 0.1$, 0.5 and 0.75, $W_a/(2a) = 0.24$, The normalized CWNs of TEo_{21} mode increase at first and then decrease with the increase of $(2a\text{-}d_a)/(2a)$.

When eccentricity $e = 0.9$, the normalized CWNs of the TEe_{31} mode decrease at first and then tend to constant with the increasing of $(2a\text{-}d_a)/(2a)$.

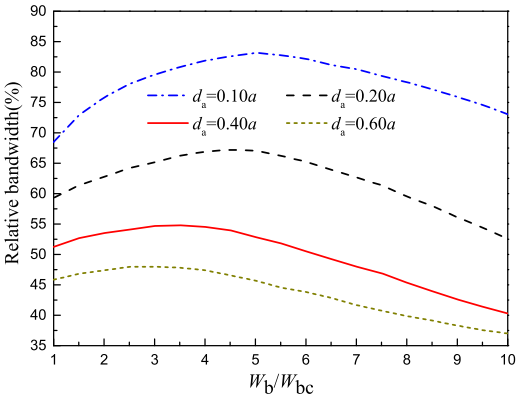

FIGURE 9. Single-mode bandwidth versus different d_a/a and W_b/W_{bc}.

With the fixed eccentricity $e = 0.5$, $W_a/a = W_b/b = 0.12$, $W_{ac}/W_a = W_{bc}/W_b$ and $L_a/a = L_b/b$, the relationship of the normalized CWNs k_ca of TEe_{11}, TEe_{21}, TEo_{11}, TEo_{21} and TMe_{01} modes with different ratio of L_a/a and W_{ac}/W_a is shown in Fig.7.

As shown in Fig.7(a), when the edge width W_{ac} is fixed, the normalized CWNs of TEe_{11}, TEe_{21} and TEo_{11} modes are determined by the ridge length L_a. The normalized CWNs of TEe_{11}, TEe_{21} and TEo_{11} modes increases with the edge width W_{ac} increasing.

As shown in Fig.7(b), the normalized CWNs of TEo_{21} and TMe_{01} modes keeps almost stable when tuning the edge width W_{ac} and the ridge length L_a. Thus, the single bandwidth of the quadruple corner-cut ridged elliptical waveguide can be broadened with sufficiently suppressing or not exciting the TEe_{21} and TEo_{11} modes.

With the fixed eccentricity $e = 0.5$, $W_{ac}/(2a) = W_{bc}/(2b) = 0.02$ and $d_a/a = d_b/b$, the relationship of the normalized CWNs k_ca of TEe_{11}, TEe_{21}, TEo_{11}, TEo_{21} and TMe_{01} modes with different ratio of d_a/a and W_b/W_{bc} ($W_a = W\text{-}W_{bc} + W_{ac}$) is shown in Fig.8.

As shown in Fig.8(a), when the ridge thickness W_b is fixed, the normalized CWNs of TEe_{11}, TEe_{21} and TEo_{11} modes are mainly determined by the ridge gap d_a. The normalized CWNs of TEe_{11}, TEe_{21} and TEo_{11} modes decrease at first and then increase with the ridge thickness W_b increasing. For the ratio of the ridge gap $d_a/a = 0.10$, the normalized CWNs of TEe_{11}, TEe_{21} and TEo_{11} modes are almost the same.

As shown in Fig.8(b), for each ridge gap d_a, the normalized CWNs of TEo_{21} mode increase at first and then decrease with the ridge thickness W_b increasing. When the ridge thickness W_b is fixed, the normalized CWNs of TEo_{21} mode are mainly determined by the ridge gap d_a.

As shown in Fig.8(c), for the ratio of the ridge gap with the $d_a/a = 0.10$, 0.20 and 0.40, the normalized CWNs of TMe_{01} mode increase with the ridge thickness W_b increasing. For the ratio of ridge gap $d_a/a = 0.60$, the normalized CWNs of TMe_{01} mode increase at first and then tend to constant with the ridge thickness W_b increasing.

Because the CWNs of TEe_{21} and TEo_{11} modes are close to that of the dominant TEe_{11} mode. Thus, when efficiently

TABLE 1. The CWN, RMSE and CPU time of the ridged elliptical waveguide with SBFEM and NSBFEM.

Boundary condition	Mode	FEM (69217)	SBFEM (33)	SBFEM (65)	SBFEM (129)	SBFEM (257)	NSBFEM (31)	NSBFEM (59)	NSBFEM (115)	NSBFEM (227)
Ey-Mx	TE_1	0.9476	09483	0.9476	0.9476	0.9476	0.9477	0.9476	0.9476	0.9476
Ex-My	TE_2	1.0107	1.0114	1.0107	1.0107	1.0107	1.0108	1.0107	1.0107	1.0107
Ex-Ey	TE_3	1.0292	1.0300	10292	1.0292	1.0292	1.0294	1.0292	1.0292	1.0292
Mx-My	TE_4	3.3709	3.3731	3.3710	3.3709	3.3709	3.3721	3.3709	3.3709	3.3709
Ey-Mx	TE_5	4.2032	4.2036	4.2032	4.2032	4.2032	4.2035	4.2032	4.2032	4.2032
Ex-My	TE_6	4.2081	4.2084	4.2081	4.2081	4.2081	4.2083	4.2082	4.2081	4.2081
Ex-Ey	TE_7	4.2094	4.2098	4.2095	4.2094	4.2094	4.2096	4.2095	4.2094	4.2094
Mx-My	TE_8	4.2488	4.2493	4.2488	4.2488	4.2488	4.2490	4.2488	4.2488	4.2488
Ey-Mx	TE_9	5.7188	5.7225	5.7190	5.7188	5.7188	5.7192	5.7190	5.7188	5.7188
Ex-My	TE_{10}	5.9678	5.9724	5.9681	5.9679	5.9678	5.9682	5.9678	5.9678	5.9678
Ex-Ey	TE_{11}	6.0389	6.0449	6.0393	6.0390	6.0389	6.0393	6.0392	6.0389	6.0389
Mx-My	TE_{12}	6.6104	6.6199	6.6109	6.6105	6.6104	6.6122	6.6104	6.6104	6.6104
Ey-Mx	TE_{13}	7.5102	7.5167	7.5108	7.5103	7.5100	7.5131	7.5102	7.5102	7.5102
Ex-My	TE_{14}	7.5597	7.5656	7.5604	7.5599	7.5597	7.5603	7.5598	7.5597	7.5597
Ex-Ey	TE_{15}	7.5713	7.5782	7.5722	7.5714	7.5713	7.5742	7.5714	7.5713	7.5713
Mx-My	TE_{16}	7.6272	7.6345	7.6281	7.6273	7.6272	7.6325	7.6274	7.6272	7.6272
Ey-Mx	TM_1	7.6400	7.6471	7.6407	7.6401	7.6400	7.6432	7.6401	7.6400	7.6400
Ex-My	TM_2	7.6400	7.6471	7.6407	7.6401	7.6400	7.6432	7.6401	7.6400	7.6400
Ex-Ey	TM_3	7.6400	7.6471	7.6407	7.6401	7.6400	7.6432	7.6401	7.6400	7.6400
Mx-My	TM_4	7.6400	7.6471	7.6407	7.6401	7.6400	7.6432	7.6401	7.6400	7.6400
Ey-Mx	TE_{17}	8.4361	8.4527	8.4371	8.4362	8.4362	8.4421	8.4362	8.4362	8.4361
Ex-My	TE_{18}	9.1474	9.1620	9.1489	9.1475	9.1474	9.1508	9.1476	9.1474	9.1474
Ex-Ey	TE_{19}	9.3253	9.3400	9.3268	9.3254	9.3253	9.3315	9.3254	9.3253	9.3253
Mx-My	TE_{20}	9.4494	9.4633	9.4504	9.4495	9.4494	9.4533	9.4496	9.4494	9.4494
Ey-Mx	TE_{21}	9.5385	9.5510	9.5393	9.5387	9.5385	9.5409	9.5388	9.5385	9.5385
RMSE(%)		\	0.5058	0.0431	0.0060	0.0012	0.0176	0.0093	0.0012	0.0002
Time(s)		\	0.21	0.74	2.26	3.67	0.23	0.93	2.56	4.39

suppressing or not exciting the TEe_{21} and TEo_{11} modes, the relative single-mode bandwidth BW can be determined by the CWNs of the TEo_{21} and TEe_{11} mode as follows:

$$BW = \frac{2\left(k_c^{\mathrm{TEo}_{21}} - k_c^{\mathrm{TEe}_{11}}\right)}{k_c^{\mathrm{TEo}_{21}} + k_c^{\mathrm{TEe}_{11}}} \times 100\% \tag{29}$$

Fig.9 shows that, the relative single-mode bandwidths are mainly determined by the ridge thickness W_b and the gap distance d_a of the QCRE waveguide. As the ratio W_b/W_{bc} increasing, the relative single-mode bandwidths increase first and then decrease. Consequently, an optimal relative single-mode bandwidth can be achieved by changing the ridge thickness, ridge gap and corner-cut edge width of the QCRE waveguide.

VI. CONCLUSION

The NURBS enhanced SBFEM has been successfully extended to analyze the QCRE waveguide. In the NURBS enhanced SBFEM, the curved boundaries and straight boundaries of the subdomains are described and discretized by NURBS and Lagrange basis function, respectively, and the spatial dimensions is reduced by one. It has been shown that, the elliptical boundary can be exactly represented by the NURBS basis function, and the accuracy and efficiency of the NURBS enhanced SBFEM are better than that of the traditional SBFEM. With the NURBS enhanced SBFEM, the corner-cut influence on the CWNs and the single-mode bandwidth have been studied in details. Moreover, the NURBS enhanced SBFEM could be extended to analyze the waveguide structure with complicated geometry in engineering problems.

REFERENCES

[1] W. Sun and C. A. Balanis, "MFIE analysis and design of ridged waveguides," *IEEE Trans. Microw. Theory Techn.*, vol. 41, no. 11, pp. 1965–1971, Nov. 1993.

[2] J.-M. Guan and C.-C. Su, "Analysis of metallic waveguides with rectangular boundaries by using the finite-difference method and the simultaneous iteration with the Chebyshev acceleration," *IEEE Trans. Microw. Theory Techn.*, vol. 43, no. 2, pp. 374–382, Feb. 1995.

[3] S. A. Sivaram and K. J. Vinoy, "Inverse multiquadric radial basis functions in eigenvalue analysis of a circular waveguide using radial point interpolation method," *IEEE Microw. Wireless Compon. Lett.*, vol. 30, no. 6, pp. 537–540, Jun. 2020.

[4] U. Balaji, "Radial mode matching analysis of ridged circular waveguides," *IEEE Trans. Microw. Theory Techn.*, vol. 44, no. 7, pp. 1183–1186, Jul. 1996.

[5] Y. Tang, J. Zhao, and W. Wu, "Mode-matching analysis of quadruple-ridged square waveguides," *Microw. Opt. Technol. Lett.*, vol. 47, no. 2, pp. 190–194, 2005.

[6] Y. Tao, Z. Shen, and G. Liu, "Efficient analysis of quadruple corner-cut ridged circular waveguide by hybrid mode-matching boundary-element method," *IEEE Trans. Magn.*, vol. 45, no. 3, pp. 1076–1079, Mar. 2009.

[7] Y. Tao, Z. Shen, and B. Zheng, "Analysis of quadruple corner-cut ridged square waveguide by hybrid mode-matching boundary-element method," *Int. J. Numer. Modelling, Electron. Netw., Devices Fields*, vol. 24, no. 1, pp. 24–35, Jan. 2011.

[8] Q. Zheng, "Analysis of a ridge waveguide family based on subregion solution of multipole theory," in *Proc. IEEE World Automat. Congr.*, Sep./Oct. 2008, pp. 1–4.

[9] M. H. Chen, G. N. Tsandoulas, and F. G. Willwerth, "Modal characteristics of quadruple-ridged circular and square waveguides (short papers)," *IEEE Trans. Microw. Theory Techn.*, vol. MTT-22, no. 8, pp. 801–804, Aug. 1974.

[10] M. Israel and R. Miniowitz, "An efficient finite element method for nonconvex waveguide based on hermitian polynomials," *IEEE Trans. Microw. Theory Techn.*, vol. MTT-35, no. 11, pp. 1019–1026, Nov. 1987.

[11] B. Schiff, "Eigenvalues for ridged and other waveguides containing corners of angle $3\pi/2$ or 2π by the finite element method," *IEEE Trans. Microw. Theory Techn.*, vol. 39, no. 6, pp. 1034–1039, Jun. 1991.
[12] P. Li, J. Liu, G. Lin, S. Lu, and P. Zhang, "Isogeometric analysis with trimming technique for quadruple arch-cut ridged circle waveguide," *Int. J. Numer. Model., Electron. Netw., Devices Fields*, vol. 30, no. 2, p. e2182, Mar. 2017.
[13] J. Liu and G. Lin, "Analysis of quadruple corner-cut ridged elliptical waveguide by scaled boundary finite element method," *Int. J. Numer. Model., Electron. Netw., Devices Fields*, vol. 25, no. 4, pp. 303–316, Jul. 2012.
[14] J. Liu, G. Lin, J. Li, and H. Zhong, "Analysis of quadruple corner-cut ridged square waveguide using a scaled boundary finite element method," *Appl. Math. Model.*, vol. 36, no. 10, pp. 4797–4809, Oct. 2012.
[15] J. P. Wolf and C. Song, "The scaled boundary finite-element method—A primer: Derivations," *Comput. Struct.*, vol. 60, nos. 1–3, pp. 191–210, 2000.
[16] C. Song and J. P. Wolf, "The scaled boundary finite-element method—A primer: Solution procedures," *Comput. Struct.*, vol. 78, nos. 1–3, pp. 211–225, 2000.
[17] Z. J. Yang, X. F. Wang, D. S. Yin, and C. Zhang, "A non-matching finite element-scaled boundary finite element coupled method for linear elastic crack propagation modelling," *Comput. Struct.*, vol. 153, pp. 126–136, Jun. 2015.
[18] D. Chen and S. Dai, "Dynamic fracture analysis of the soil-structure interaction system using the scaled boundary finite element method," *Eng. Anal. Boundary Elements*, vol. 77, pp. 26–35, Apr. 2017.
[19] J.-B. Li, X. Gao, X.-A. Fu, C. Wu, and G. Lin, "A nonlinear crack model for concrete structure based on an extended scaled boundary finite element method," *Appl. Sci.*, vol. 8, no. 7, p. 1067, Jun. 2018.
[20] J. Liu, G. Lin, F. Wang, and J. Li, "The scaled boundary finite element method applied to electromagnetic field problems," *IOP Conf. Ser., Mater. Sci. Eng.*, vol. 10, Jun. 2010, Art. no. 12245.
[21] C. Li and L. Tong, "2D fracture analysis of magnetoelectroelastic composites by the SBFEM," *Compos. Struct.*, vol. 132, pp. 984–994, Nov. 2015.
[22] J. Liu, P. Zhang, G. Lin, W. Wang, and S. Lu, "Solutions for the magneto-electro-elastic plate using the scaled boundary finite element method," *Eng. Anal. Boundary Elements*, vol. 68, pp. 103–114, Jul. 2016.
[23] W. Yi, L. Gao, and H. Zhiqiang, "Novel nonreflecting boundary condition for an infinite reservoir based on the scaled boundary finite-element method," *J. Eng. Mech.*, vol. 141, no. 5, 2015, Art. no. 4014150.
[24] H. Xu, D. Zou, X. Kong, and Z. Hu, "Study on the effects of hydrodynamic pressure on the dynamic stresses in slabs of high CFRD based on the scaled boundary finite-element method," *Soil Dyn. Earthq. Eng.*, vol. 88, pp. 223–236, Sep. 2016.
[25] J. Liu, J. Li, P. Li, G. Lin, T. Xu, and L. Chen, "New application of the isogeometric boundary representations methodology with SBFEM to seepage problems in complex domains," *Comput. Fluids*, vol. 174, pp. 241–255, Sep. 2018.
[26] H. Zhong, H. Li, E. T. Ooi, and C. Song, "Hydraulic fracture at the dam-foundation interface using the scaled boundary finite element method coupled with the cohesive crack model," *Eng. Anal. Boundary Elements*, vol. 88, pp. 41–53, Mar. 2018.
[27] Y. Li, H. Zhong, L. Pang, and Z. Hu, "Influence of the water pressure distribution along crack faces on seismic fracture modeling of a dam-reservoir-foundation system," *Eng. Anal. Boundary Elements*, vol. 101, pp. 252–269, Apr. 2019.
[28] F. Wang, G. Lin, Y.-H. Zhou, and D.-H. Chen, "Element-free Galerkin scaled boundary method based on moving Kriging interpolation for steady heat conduction analysis," *Eng. Anal. Boundary Elements*, vol. 106, pp. 440–451, Sep. 2019.
[29] T. J. R. Hughes, J. A. Cottrell, and Y. Bazilevs, "Isogeometric analysis: CAD, finite elements, NURBS, exact geometry and mesh refinement," *Comput. Methods Appl. Mech. Eng.*, vol. 194, nos. 39–41, pp. 4135–4195, Oct. 2005.
[30] T. Yu, B. Chen, S. Natarajan, and T. Q. Bui, "A locally refined adaptive isogeometric analysis for steady-state heat conduction problems," *Eng. Anal. with Boundary Elements*, vol. 117, pp. 119–131, Aug. 2020.
[31] L. Dedè, M. J. Borden, and T. J. R. Hughes, "Isogeometric analysis for topology optimization with a phase field model," *Arch. Comput. Methods Eng.*, vol. 19, no. 3, pp. 427–465, Sep. 2012.
[32] L. De Lorenzis, P. Wriggers, and T. J. R. Hughes, "Isogeometric contact: A review," *GAMM-Mitteilungen*, vol. 37, no. 1, pp. 85–123, Jul. 2014.
[33] Y. Zhang, G. Lin, Z.-Q. Hu, and J. Liu, "Isogeometric analysis for elliptical waveguide eigenvalue problems," *J. Central South Univ.*, vol. 20, no. 1, pp. 105–113, Jan. 2013.
[34] A. Buffa, G. Sangalli, and R. Vázquez, "Isogeometric analysis in electromagnetics: B-splines approximation," *Comput. Methods Appl. Mech. Eng.*, vol. 199, nos. 17–20, pp. 1143–1152, Mar. 2010.
[35] Y. Zhang, G. Lin, and Z. Q. Hu, "Isogeometric analysis based on scaled boundary finite element method," *IOP Conf. Ser., Mater. Sci. Eng.*, vol. 10, Jun. 2010, Art. no. 12237.
[36] G. Lin, Y. Zhang, Z. Hu, and H. Zhong, "Scaled boundary isogeometric analysis for 2D elastostatics," *Sci. China Phys., Mech. Astron.*, vol. 57, no. 2, pp. 286–300, Feb. 2014.
[37] G. Lin, B. Xue, and Z. Hu, "A mortar contact formulation using scaled boundary isogeometric analysis," *Sci. China Phys., Mech. Astron.*, vol. 61, no. 7, Jul. 2018, Art. no. 74621.
[38] B. Xue, G. Lin, and Z. Hu, "Scaled boundary isogeometric analysis for electrostatic problems," *Eng. Anal. Boundary Elements*, vol. 85, pp. 20–29, Dec. 2017.
[39] P. Li, J. Liu, G. Lin, P. Zhang, and G. Yang, "A NURBS-based scaled boundary finite element method for the analysis of heat conduction problems with heat fluxes and temperatures on side-faces," *Int. J. Heat Mass Transf.*, vol. 113, pp. 764–779, Oct. 2017.
[40] S. Natarajan, J. Wang, C. Song, and C. Birk, "Isogeometric analysis enhanced by the scaled boundary finite element method," *Comput. Methods Appl. Mech. Eng.*, vol. 283, pp. 733–762, Jan. 2015.
[41] L. Piegl and W. Tiller, *The NURBS Book*, 2nd ed. New York, NY, USA: Springer-Verlag, 1997.
[42] C. Song, "The scaled boundary finite element method in structural dynamics," *Int. J. Numer. Methods Eng.*, vol. 77, no. 8, pp. 1139–1171, Feb. 2009.

BINGHAN XUE was born in Henan, China, in 1991. He received the Ph.D. degree in hydraulic structure engineering from the Dalian University of Technology, in 2018. He is currently a Lecturer with the School of Water Conservancy Engineering, Zhengzhou University, Zhengzhou, China.

His research interests include scaled boundary finite element method, isogeometric analysis, and their applications in electromagnetic field and civil engineering.

JIANWEI LEI was born in Inner Mongolia, China, in 1993. He received the B.S. degree in road bridge and river-crossing engineering from Zhengzhou University, Zhengzhou, China, in 2016, where he is currently pursuing the Ph.D. degree in safety and protection engineering.

His research interests include microwave components, GPR, and numerical simulation methods, such as finite-difference time-domain method and sympletic methods.

SHAOKUN MA was born in Hunan, China, in 1972. He received the Ph.D. degree in geotechnical engineering from Tongji University, in 2008. He is currently a Professor and the Head of the Department of Geotechnical Engineering, Guangxi University, Nanning, China.

His research interests include waveguide antennas, underground engineering, and centrifuge modeling.

MINGRUI DU was born in Henan, China, in 1989. He received the Ph.D. degree in geotechnical engineering from the China University of Mining and Technology, in 2018. He is currently an Associate Professor with the School of Water Conservancy Engineering, Zhengzhou University, Zhengzhou, China.

His research interests include molecular dynamics simulation theory, finite element method, and their application in physic field.